CrossMark

ROYAL
AERONAUTICAL
SOCIETY

REGULAR PAPER

Analysis and optimisation design on damping orifice of oleo-pneumatic landing gear

S. Gan[2] , X. Fang[2] and X. Wei[1,*]

[1]Key Laboratory of Fundamental Science for National Defense-Advanced Design Technology of Flight Vehicle, Nanjing University of Aeronautics and Astronautics, Nanjing, Jiangsu, 210016, China and [2]State Key Laboratory of Mechanics and Control of Mechanical Structures, Nanjing University of Aeronautics and Astronautics, Nanjing, Jiangsu, 210016, China
Corresponding author. Email: wei_xiaohui@nuaa.edu.cn

Abstract
This paper investigates the feasibility of improving the aircraft landing performance by design the damping orifice parameters of the landing gear using lattice Boltzmann method coupled with the response surface method. The LBM is utilised to simulate characteristics of the damping orifice after model validation. The numerical model of the landing gear using simulated damping force is validated by single landing gear drop test. Based on the numerical model and the response surface functions, the sensitivity analysis and the optimisation design are performed. The maximum error of mean velocity simulated using LBM with experimental data is 7.07% for sharp-edged orifices. Moreover, the numerical model predicts the landing responses adequately, the maximum error with drop test data is 2.51%. The max overloading of the aircraft decreases by 5.44% after optimisation, which proves that this method is feasible to design the damping orifice for good landing performance.

Nomenclature

A_0	area of the orifice
A_1	area of the 1–1 section
A_a	gas compression area
A_c	area of the jet at the vena contracta
C_c	contraction coefficient
C_d	discharge coefficient
C_T	vertical damping deformation coefficient
C_v	velocity coefficient
C_x	LES model dependent constant
d_0	orifice diameter
d_c	oil compression diameter
$f(z_2)$	tire vertical static force
F	total force in the shock strut
F_a	air spring stiffness force
F_C	magnitude of Coulomb friction
F_f	friction force
F_h	hydraulic force
F_{max}	max total force in the shock strut
F_{nf}	journal friction force
F_S	magnitude of static friction
F_{sf}	seal friction force
F_V	vertical ground force acting on the tire

g	gravitational constant
G_{ij}^d	gradient velocity tensor
l_0	orifice length
m_1	sprung mass
m_2	unsprung mass
OL	max overloading of the sprung mass
P_0	initial gas pressure
P_1	pressure at the 1–1 section
P_{atm}	atmospheric pressure
P_b	backpressure
P_c	pressure at the c–c section
Q	flow rate through the orifice
sgn	signum function
S	shock absorber stroke
$\bar{S}_{ij}$	rate-of-strain tensor
S_{max}	maximum shock absorber stroke
v	relative velocity
v_0	tolerance velocity
v_1	mean velocity of the fluid at the 1–1 section
v_c	mean velocity of the fluid at the c–c section
v_s	Stribeck velocity
V_0	initial gas volume
z_1	vertical displacement of the sprung mass
Z_1	height of the 1–1 section
z_2	vertical displacement of the unsprung mass
Z_2	height of the c–c section
γ	gas polytropic exponent
v_t	turbulent eddy viscosity
ξ	resistance coefficient
ΔP	pressure difference
Δx	lattice spacing
η_s	shock absorber energy absorption efficiency
μ_{sf}	seal friction coefficient
μ_w	ground friction coefficient
ρ	density of the oil
$\bar{\varpi}$	LES model operator

1.0 Introduction

The landing gear is an inevitable system for the aircraft. It absorbs the energy of the landing impact and carries the aircraft weight at all ground operations, including take-off, taxiing, and towing [1]. The two-degree-freedom model was introduced to analyse landing gear dynamic responses during aircraft landing in 1953 [2] and is still used recently in landing gear buffer analysis [3, 4]. The damping orifice is the key part of the landing gear shock absorber for dissipating the landing impact energy. The max force in the landing gear strut during landing process results from the hydraulic force induced by the damping orifice, which directly causes the max overloading of the aircraft. Since the hydraulic force is related to the landing response, the design of the damping orifice parameters is workable for good landing performance.

The research methodology of studying the characteristics of the orifice can be typically classified into three categories, namely, the engineering estimation method [5], the experimental and empirical method [6, 7], and the computational fluid dynamics (CFD) simulation method [8, 9]. The engineering estimation method sets the discharge coefficient of the orifice to be a constant number, which needs the experiment data to validate. The experimental method is accurate to measure the discharge coefficient
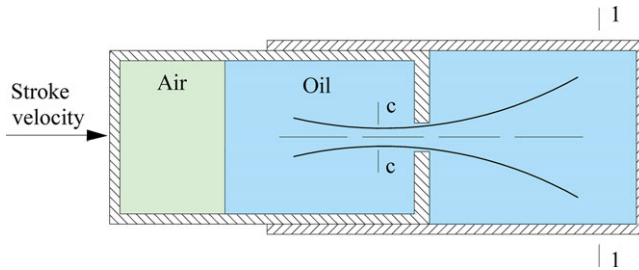
Figure 1. *Schematic diagram of orifice flow.*

for a specific orifice structure, such as sharp-edged orifice [6, 10], taper inlet orifice [11, 12], and round inlet orifice [13]. But the experimental result is only effective for the orifice with the specific type and parameter. As the development of CFD, it is feasible to obtain the discharge coefficient of the orifice by simulation. The Navier-Stokes solvers using the Reynolds Averaged Navier-Stokes (RANS) turbulence models are able to solve complex engineering problems [14]. However, the numerical stability of these mesh-based solutions is limited by the mesh quality which requires large time cost to modify and verify.

The LBM, a particle-based solution, presents an alternative and promising numerical scheme for simulating fluid flows [15]. The scheme is particularly effective in fluid flow applications involving complex boundaries [16, 17] and interfacial dynamics [18, 19]. Theoretical analysis of the high Reynolds number separation flow inside the damping orifices to calculate the hydraulic force is basically impossible. The advantages of LBM in calculating complex flows [20, 21] make it a potentially viable CFD solution. The response surface method (RSM) is a collection of statistical and mathematical techniques [22], which can reduce the time and computational expense for analysis and design. This method is applied in some complex engineering applications, such as aircraft [23] and lunar lander [24, 25] design. The parametric analysis and optimisation design of the damping orifice need many times calculation of the hydraulic force using the LBM which will take a lot of time. To obtain an advisable layout of the orifice quickly, it is necessary to use the LBM coupled with the RSM to research the parameters of the damping orifice.

The content of this work is organized as follows. First, Subsection 2.1 introduces the basic feature of the damping orifice. The results of a computation example using the LBM are compared with the published experimental data. And the analysis of the damping orifice of landing gear is carried out in Subsection 2.3. Then, Section 3 establishes the numerical model of the landing gear and validates the model by the landing gear drop test. Moreover, Section 4 uses the response surface method to implement the response surface functions construction, sensitivity analysis, and optimisation design based on the numerical model coupled with the LBM. Finally, Section 5 summarises the main conclusions of this work.

2.0 Orifice characteristic analysis

2.1 Basic feature of damping orifice

The oleo-pneumatic landing gear uses the small oil damping orifice to dissipate the aircraft landing impact energy. The oil flow shrinks when it passes through the small hole from a bigger cross-section and forms a vena contracta behind the small hole, as shown in Fig. 1. Bernoulli's equation is applied to 1–1 section and c–c section:

$$\frac{P_1}{\rho g} + \frac{v_1^2}{2g} + Z_1 = \frac{P_c}{\rho g} + (1+\xi)\frac{v_c^2}{2g} + Z_c \tag{1}$$

where P_1 and P_c are the pressure at the 1–1 section and c–c section, g indicates the gravitational constant, v_1 and v_2 are the mean velocity of the fluid at the 1–1 section and c–c section, Z_1 and Z_2 are the height of the 1–1 section and c–c section, ξ is the resistance coefficient, ρ is the density of the oil.

Consider the flow occurs on a horizontal surface, so the gravitational effect can be ignored. Moreover, the area of the jet at the vena contracta usually is much smaller than the area of the incoming flow section, the mean velocity of the fluid in the 1–1 section v_1 is much smaller than the mean velocity of the fluid in the c–c section v_c. Therefore, the mean velocity of the fluid in the c–c section is presented by the equation

$$v_c = \frac{1}{\sqrt{1+\xi}}\sqrt{\frac{2\,(P_1 - P_c)}{\rho}} = C_v\sqrt{\frac{2\Delta P}{\rho}} \tag{2}$$

where C_v is the velocity coefficient, ΔP is the pressure difference.

The contraction coefficient C_c is defined as $C_c = A_c/A_0$, where A_c is the area of the jet at the vena contracta, A_0 is the area of the orifice. The flow rate through the orifice can be expressed as

$$Q = V_c A_c = C_c C_v A_0\sqrt{\frac{2\Delta P}{\rho}} = C_d A_0\sqrt{\frac{2\Delta P}{\rho}} \tag{3}$$

where C_d is the discharge coefficient. The hydraulic force can be calculated through the pressure difference and the compression area, which can be expressed as

$$F_h = \Delta P A_1 = \frac{\rho A_1 Q^2}{2 C_d^2 A_0^2} \tag{4}$$

where F_h is the hydraulic force, A_1 is the area of the 1–1 section which is the oil compression area. The flow rate Q is the product of the stroke velocity and the area of the 1–1 section. All the values of the parameters in Equation (4) are determined in a specific landing gear structure and landing condition, except for the discharge coefficient. The discharge coefficient is related to the orifice structure, flow rate, pressure difference, and fluid property, which cannot be obtained by theoretical calculations. The recommended discharge coefficient value for sharp-edged orifice is 0.7–1.0 in the engineering estimation method. The CFD methods can be used to calculate the discharge coefficient according to the given orifice structure.

2.2 A computation example: sharp-edged orifice

In this subsection, the flow characteristics of sharp-edged orifice are simulated using the LBM. The comparison of the simulation results with the published results is conducted to verify the applicability of the LBM in calculating the flow characteristics of orifices. The simulation condition is set according to the Ref. [10]. A three-dimensional model of the sharp-edged orifice is established and calculated using OpenLB package, which is a C++ library providing a flexible framework for lattice Boltzmann simulations [26]. The schematic of cross-section of the sharp-edged orifice is shown in Fig. 2. The details of the orifices used for the simulation are given in Table 1.

The collision operator is based on the multiple-relaxation-time [27] scheme. The finite difference velocity gradients boundary method [28] is selected in this simulation. The boundary conditions imposed on calculation domain of the damping orifice in the numerical simulation are listed in Table 2, and the detailed position of each boundary is shown in Fig. 3. To simulate this case, a single-phase internal flow set up with the isothermal model is selected. The default setup of material parameters of the water is adopted.

The lattice size in the fluid domain is organised into three levels, the lattice size around the orifices set to be the minimum value of the three levels. The grid independence is checked using four different lattice sizes under orifice 3 with a pressure drop of 1.0MPa, as summarised in Table 3. The fine lattice level is selected for the simulation and the lattice setup in symmetrical profile view is shown in Fig. 3.

The turbulence model implemented in LBM is based on Large Eddy simulation (LES), which is less computationally expensive to implement in the LBM framework than in the Navier-Stokes solvers. The LES introduces a turbulent eddy viscosity v_t to model the turbulence [29], which is defined as:

Table 1. *Details of orifices*

Orifice No.	Orifice diameter (mm)	Orifice l/d
1	0.6	1.67
2	0.6	3.33
3	0.6	6.67
4	1.4	1.43
5	1.4	4.29
6	1.4	10.0

Table 2. *Simulation boundary conditions setting*

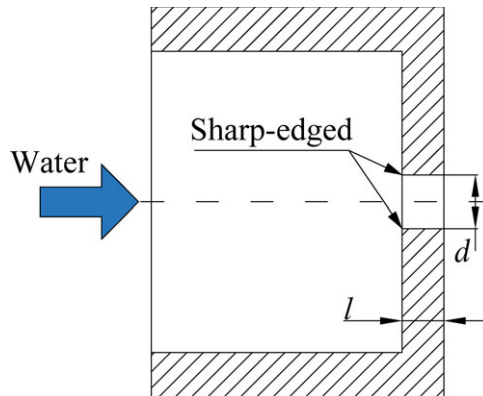| Location	Condition	Value
Inlet	Pressure inlet	0–2.0MPa
Wall	No slip wall	Zero velocity on three axes
Outlet	Pressure outlet	0MPa

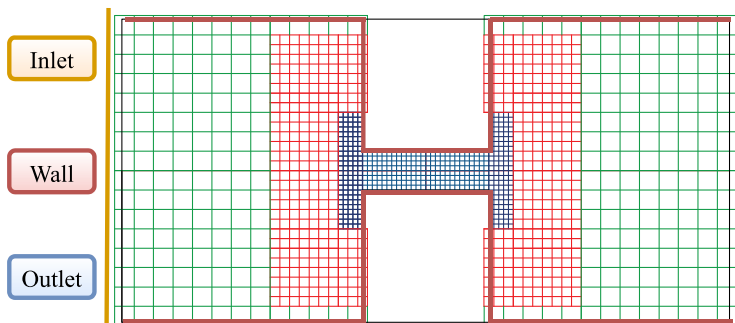**Figure 2.** *Schematic of sharp-edged orifice.*

Figure 3. *Lattice structure with different lattice resolution.*

$$v_t = C_x^2 \Delta x^2 \bar{\bar{\varpi}} \tag{5}$$

where C_x is the LES model dependent constant, Δx denotes the lattice spacing, and $\bar{\bar{\varpi}}$ is the LES model operator. Three turbulence models are selected for simulation in LBM, namely, Smagorinsky model [30], dynamic Smagorinsky model [31], and wall-adapting local eddy-viscosity (WALE) model [32].

Table 3. *Grid independence check information*

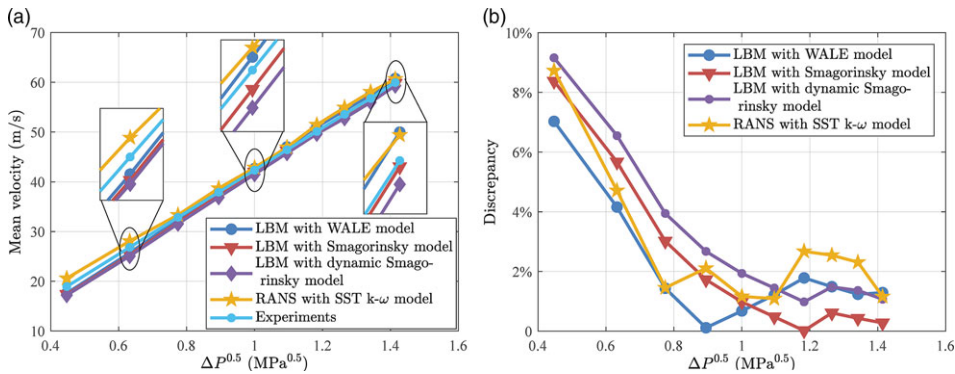| Level	Minimum lattice size (mm)	Elements	Mean velocity (m/s)
Extra-Coarse	0.12	8, 450	30.02
Coarse	0.1	13, 164	38.17
Medium	0.09	15, 704	36.61
Fine	0.08	21, 864	36.08

Figure 4. *Comparison of simulated and experimental results (a) variation of velocity with* $\Delta P^{0.5}$ *(b) discrepancy.*

The model operator for Smagorinsky model is given by:

$$\bar{\varpi} = \sqrt{2\bar{S}_{ij}\bar{S}_{ij}}$$

$$\bar{S}_{ij} = \frac{1}{2}\left(\frac{\partial \bar{u}_i}{\partial x_j} + \frac{\partial \bar{u}_j}{\partial x_i}\right) \tag{6}$$

where $\bar{S}_{ij}$ is the rate-of-strain tensor for the resolved scale. In the dynamic Smagorinsky model, the LES constant varies in space as well as time. The WALE model is based on the square of the gradient velocity tensor G_{ij}^d, which is defined as follow:

$$\bar{\varpi} = \frac{\left(G_{ij}^d G_{ij}^d\right)^{3/2}}{\left(\bar{S}_{ij}\bar{S}_{ij}\right)^{5/2} + \left(G_{ij}^d G_{ij}^d\right)^{5/4}}$$

$$G_{ij}^d = \frac{1}{2}\left(\bar{g}_{ij}^2 + \bar{g}_{ji}^2\right) - \frac{1}{3}\delta_{ij}\bar{g}_{kk}^2, \bar{g}_{ij} = \frac{\partial \bar{u}_i}{\partial x_j} \tag{7}$$

The LES constants are set to be 0.325, 0.12 and 0.12 for WALE model, Smagorinsky model, and initial value of the dynamic Smagorinsky model, respectively. In order to compare the ability of mesh-based solvers and LBM to handle such flow problems, a numerical simulation is conducted in software Fluent using shear-stress transport (SST) k-ω turbulence model [33] in the framework of RANS method. The mesh scheme approximately with around 87,000 cells is used after mesh independence check. The boundary conditions setting is the same as set in LBM and other setups in Fluent follow the Ref. [8]. The experimental data published in the Ref. [10] are utilised to compare with the simulation results at different specific orifices. The mean velocity variations at the exit of the orifice with the square root of the pressure drop ($\Delta P^{0.5}$) obtained from four kinds of simulation for orifice 1 are shown in Fig. 4.

As shown in Fig. 4(a), the results of all four simulation models show that the mean velocity increases linearly with the square root of the pressure drop, in line with the trend of the experimental results. The

Table 4. *Details of damping orifice*

Parameter	Description	Value
d_0	Orifice diameter (mm)	3.8
l_0	Orifice length (mm)	5.0
d_c	Oil compression diameter (mm)	28
P_b	Backpressure (MPa)	0.85

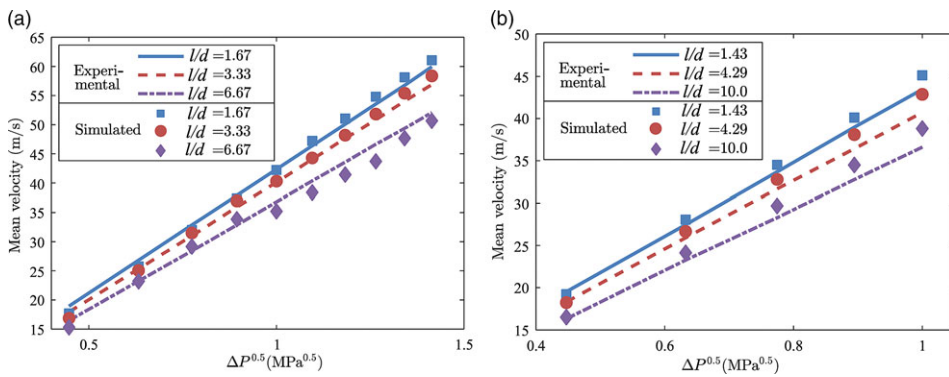***Figure 5.*** *Variation of velocity with $\Delta P^{0.5}$ (a) $d = 0.6mm$ (b) $d = 1.4mm$.*

results of all four simulation models differed very little from the experimental results. The difference between several results is larger at low pressure drop, which can be seen in Fig. 4(b). A comparison of the absolute values of the relative errors with experimental results is presented in Fig. 4(b). The errors in the results of several simulations are within acceptable limits, with a maximum error of 9.16%. The LBM with WALE model has the lowest maximum error value of 7.03%.

The full comparison shows that both LBM and traditional CFD can simulate the small-hole contraction problem very well. In LBM simulation, the WALE turbulence model can better simulate the flow characteristics at different flow rates. The calculation time for ten data points using LBM with WALE model and traditional CFD method is 25 and 34 min respectively with the same computational power. Further, no need for mesh generation in the LBM is time-saving for the simulation implementation. All the orifices listed in Table 1 are simulated using LBM with WALE turbulence model. The mean velocity variations with $\Delta P^{0.5}$ for two orifice diameters are shown in Fig. 5.

Figure 5 shows that the simulated results using the LBM have good agreement with the experimental results under all six orifice conditions. The maximum relative error is 7.07% at orifice 3 with 0.2MPa pressure drop condition, which is deemed to be acceptable for engineering applications. Therefore, the LBM with WALE turbulence model can well simulate the flow characteristics of the sharp-edged orifice.

2.3 Damping orifice analysis

In this subsection, the flow characteristics of the sharp-edged damping orifice of landing gear are simulated using LBM to obtain the hydraulic force for calculating the aircraft landing response in landing process. The inlet boundary condition is changed to the mass flow inlet, with the value calculated by stroke velocity and oil compression area. The simulation setup is the same as mentioned in Subsection 2.2. The minimum lattice size around the orifice is set to be 0.18mm. The details of the damping orifice are listed in Table 4. The density and kinematic viscosity of the oil are 837kg/m³ and 13.85m²/s at the temperature of 40, respectively.
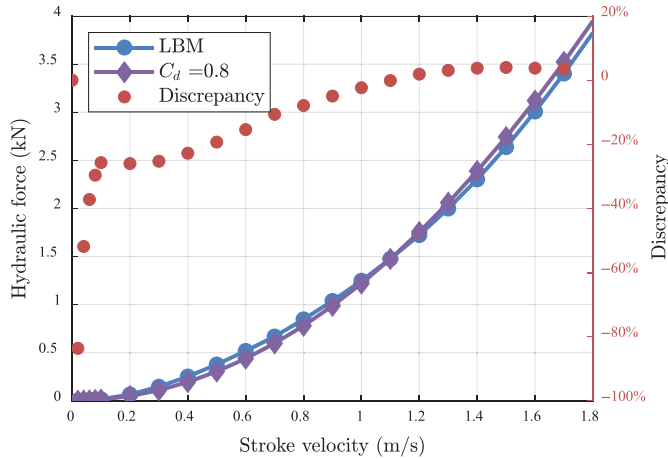
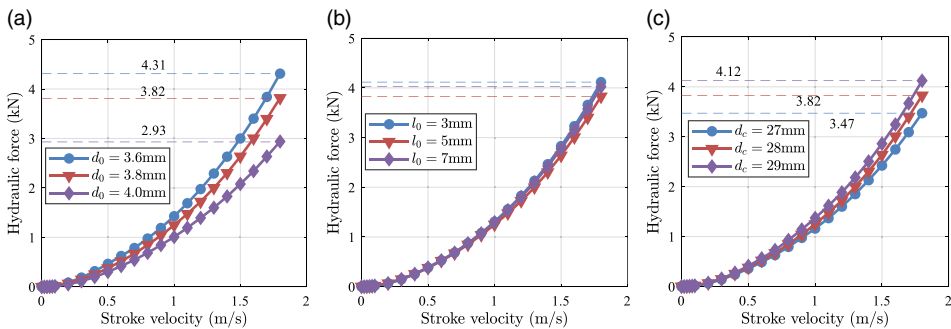**Figure 6.** *Hydraulic force results comparison.*

Figure 7. *Variation of the hydraulic force versus stroke velocity with different parameters (a) oil compression diameter (b) orifice length (c) orifice diameter.*

The comparison of the hydraulic force results calculated by the LBM and the engineering estimation method is presented in Fig. 6. The two results generally have a good agreement, except for the different offset direction between the low stroke velocity and the high stroke velocity. This means that the calculation result of C_d using the LBM is lower than 0.8 at the low stroke velocity and higher than 0.8 at the high stroke velocity. Although the discrepancies at the low stroke velocity are considerably high, namely, the max value is -83.38% at 0.02m/s stroke velocity, the low value of the hydraulic force at the low stroke velocity causes a little effect on the landing responses. This deviation in the engineering estimation method still affects the prediction accuracy of the aircraft landing responses.

The influence of the parameters of the orifice on the hydraulic force is analysed. The hydraulic forces of the orifice with different values of the orifice diameter, the orifice length, and the oil compression diameter, are calculated using the LBM, which is shown in Fig. 7. Figure 7(a) shows the influence of the orifice diameter on the hydraulic. It can be seen that the 0.2mm offset of the orifice diameter will bring about a variation of 0.89kN in the hydraulic force and the hydraulic force decreases with the increment of the orifice diameter. As shown in Fig. 7(b), the change of the orifice length from 3mm to 7mm leads to a small variety in the hydraulic force. But the variation trend is nonlinear with the increment of the orifice length in a limited interval. Figure 7(c) denotes that the hydraulic force decreases with the decrement of the oil compression diameter.
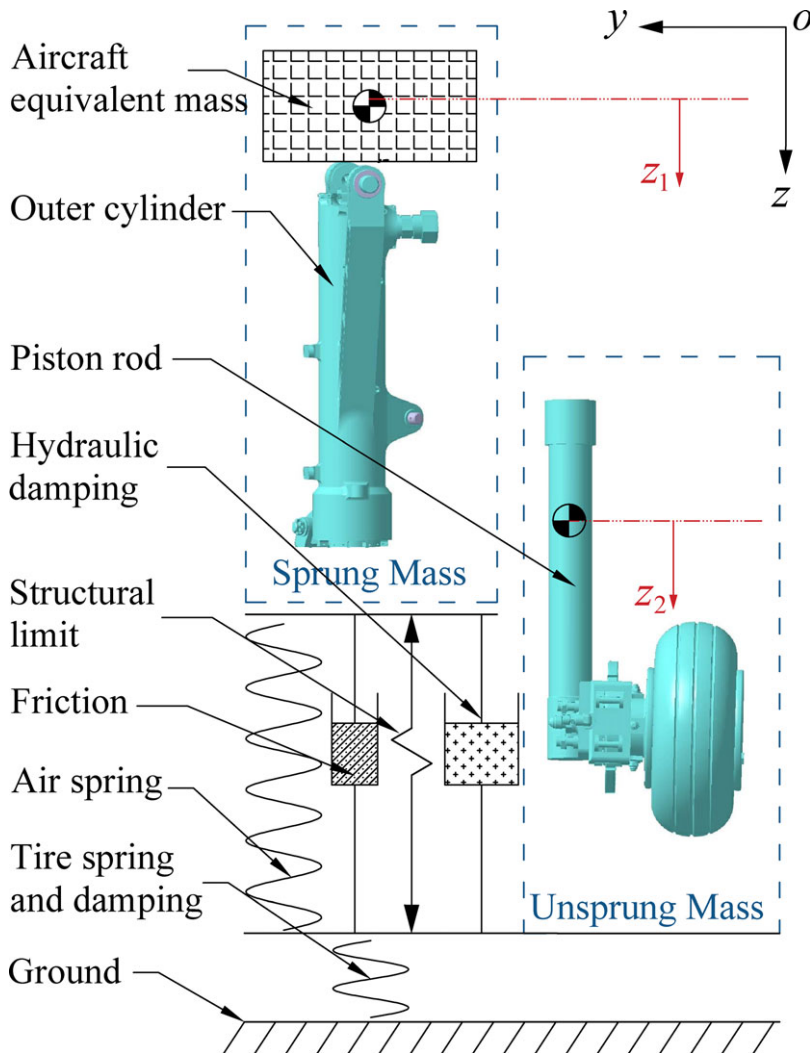
Figure 8. *Schematic of the landing gear with two degrees of freedom.*

3.0 Landing gear modelling and validating

3.1 Landing gear dynamics model

The dynamics landing gear model is necessary for predicting aircraft landing responses. A oleo-pneumatic main landing gear is selected as the research object, and a two-degrees-of-freedom spring damping model [2] is established, as shown in Fig. 8. The sprung mass includes the fuselage and the structure above the outer cylinder of the landing gear, and the unsprung mass consists of the other structure of the landing gear below the shock absorber piston rod. The oleo-pneumatic shock absorber consists of upper and lower chambers separated by orifices and the metering pin. The upper part of the upper chamber is filled with pressurised nitrogen to provide the air spring, and the other spaces of the two chambers are filled with oil to provide the damping.

According to the mathematical model shown in Fig. 8, the dynamic equilibrium governing equations of motion for the main landing gear is written as

$$\begin{cases} m_1\ddot{z}_1 = m_1g - F_a - F_h - F_f \\ m_2\ddot{z}_2 = -F_V + m_2g + F_a + F_h + F_f \end{cases} \tag{8}$$

where m_1 and m_2 indicate the sprung mass and the unsprung mass, z_1 and z_2 denote the vertical displacement of the sprung mass and unsprung mass, F_a, F_h, and F_f represent the air spring stiffness force, oil damping force, and friction force in the absorber strut, respectively. F_V is the vertical ground force acting on the tire.

The air spring stiffness force is related to initial gas volume and pressure closely, the equation can be expressed as

$$F_a = A_a \left[P_0 \left(\frac{V_0}{V_0 - A_aS} \right)^\gamma - P_{atm} \right] \tag{9}$$

where A_a is the gas compression area, P_0 is the initial gas pressure, V_0 is the initial gas volume, S is the shock absorber stroke, γ is the gas polytropic exponent, and P_{atm} is the atmospheric pressure. The calculation of the oil damping force is stated in Equation (4).

The friction forces in the strut contain the journal friction force and seal friction force. The journal friction force is induced by the normal force acting on the bearing area. The seal friction force results from the friction of internal seals in the shock absorber depends on the internal gas pressure. The friction forces in the shock strut are described by equation

$$F_f = F_{nf} + F_{sf} \tag{10}$$

where F_{nf} is the journal friction force, and F_{sf} is the seal friction force. The seal friction force depends on the internal gas pressure [34], is expressed as

$$F_{sf} = -\mu_{sf}F_a \text{sgn}(\dot{s}) \tag{11}$$

where μ_{sf} is the seal friction coefficient, and sgn is the signum function.

The journal friction force is the product of the friction coefficient and the normal force. The model with the Stribeck effect reveals that the friction force decreases continuously with the increase of relative velocity from zero velocity [35]. To eliminate the numerical issues at zero velocity, a finite slope model is established to replace the discontinuity at zero velocity, as shown in Fig. 9. The model utilised in this work can be expressed by the following equations

$$F_{nf} = \begin{cases} F_S \left| \frac{v}{v_0} \right| sgn(v) & if \ |v| < v_0 \\ \left(F_C + (F_S - F_C) e^{-\frac{|v|-v_0}{v_s}\delta} \right) \text{sgn}(v) & if \ |v| \geq v_0 \end{cases} \tag{12}$$

where F_S and F_C represent the magnitude of static friction and Coulomb friction, respectively. v is the relative velocity, v_s is the Stribeck velocity, v_0 is the tolerance velocity, δ is an exponent which depends on the geometry of the contacting surfaces, often considered to be equal to 2.

The vertical ground force results from the compression of the tire after touching the ground. A semi-empirical computational model [36] can be described by the equation

$$F_V = (1 + C_T Z_2) f(Z_2) \tag{13}$$

where C_T is the tire vertical damping deformation coefficient, $f(z_2)$ is the tire vertical static force corresponding to the tire compression amount obtained from the static compression test.

The longitudinal ground force is the friction load caused by the relative rotation of the tire and the ground. Its magnitude is related to the vertical ground force and the ground friction coefficient, which are given by

$$F_D = \mu_w F_V \tag{14}$$

where μ_w is the ground friction coefficient with typical values ranging from 0.4 to 0.9, which depends on tire angular velocity, tire-ground contact pressure, and runway condition.
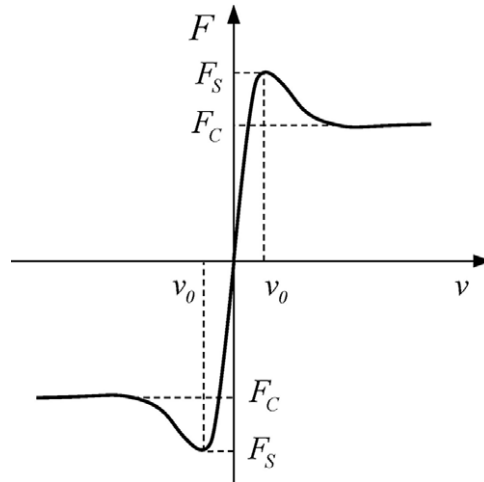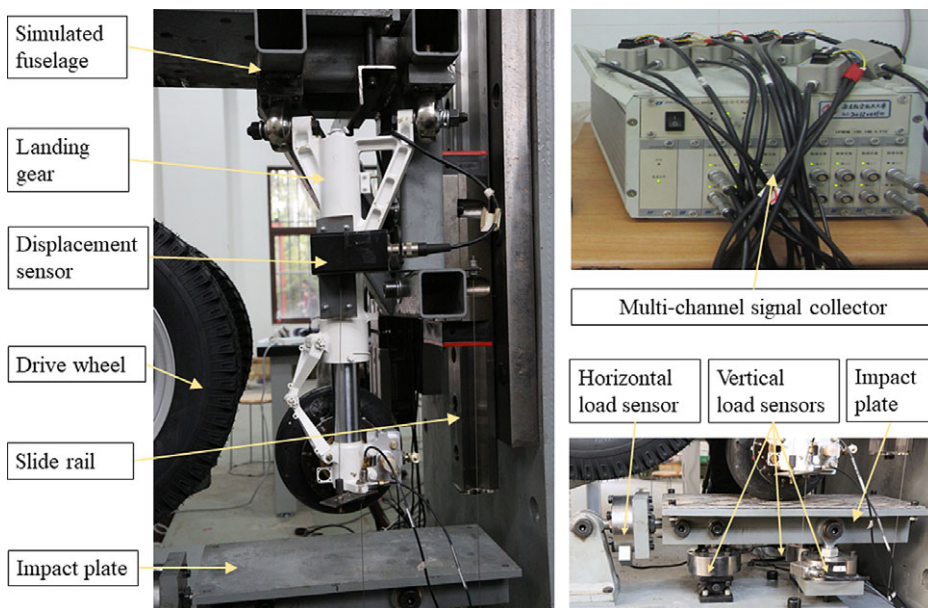
Figure 9. *Representation of Stribeck curves.*

Figure 10. *Drop test system of the single landing gear.*

3.2 Drop test and model validation

The accuracy of the numerical model of the landing gear for predicting the dynamics landing responses is validated by the drop test in this subsection. A single landing gear drop test system is conducted as shown in Fig. 10. The test system consists of the fixed platform, sliding rail, simulated fuselage, drive wheel, impact plate, displacement sensors, load sensors, and data signal collector. The fuselage and the stall points of the landing gear are simulated by the truss structure which can glide on the vertical slide rail. The descending velocity of the aircraft landing is imitated by the fixed height free fall. A suitable rough plate is installed on the impact plate to simulate the dry runway.

The various response data are collected in the buffering process, including the displacement of the sprung mass and the unsprung mass, sprung mass acceleration, ground vertical force and longitudinal

Table 5. *Landing condition properties*

Info.	Value
Sprung mass (kg)	151.83
Unsprung mass (kg)	2.85
Vertical descending velocity at initial contact (m/s)	1.8
Longitudinal velocity at initial contact (linear velocity of tire) (m/s)	65.8

Table 6. *Landing gear parameters definition and value*

Parameter	Description	Value
γ	Gas polytropic coefficient	1.3
C_d	Orifice discharge coefficient	0.8
	Fluid density (kg/m)	837
P_0	Initial gas pressure in shock strut chamber (MPa)	0.85
V_0	Initial gas volume (mm³)	129.5

Table 7. *Comparison of simulated and drop test results*

		LBM		Engineering estimation	
Info.	Test result	Result	Error (%)	Result	Error (%)
Ground vertical force (kN)	4.97	4.96	−0.27	4.96	−0.52
Ground longitudinal force (kN)	1.46	1.50	2.51	1.52	3.98
Shock absorber stroke (mm)	73.85	72.42	−1.94	71.67	−2.95
Sprung mass displacement (mm)	92.52	93.93	1.53	92.93	0.44
Unsprung mass displacement (mm)	21.56	21.53	−0.14	21.35	−0.97

force, and shock absorber stroke. The stroke is measured by a displacement sensor mounted on the landing gear. The longitudinal force load sensor is mounted horizontally ahead of the impact plate. The vertical ground force is measured by the load sensors installed vertically at the bottom of the impact plate. The two ends of the all vertical load sensors are connected by a revolute pair to retain the unrestraint of the longitudinal degree of the impact plate. A multi-channel signal collector is used to acquire real-time test data of each dynamic response.

The landing condition properties are shown in Table 5. The calculation results of the numerical model are obtained using the same values of landing gear parameters as the drop test, and the parameter values used in this work are shown in Table 6.

The LBM and the engineering estimation method are used to calculate the hydraulic force in the numerical model. The discharge coefficient is set to be 0.8 in the engineering estimation method. To verify the accuracy of the numerical model, the comparison of the landing responses obtained from the drop test with the results of numerical model calculated in MATLAB is shown in Table 7 and Fig. 11. Table 7 compares the landing gear dynamics response results of the two numerical method simulations and the drop test. The ground vertical force and shock absorber stroke are two crucial dynamic responses of landing gear in landing process [37]. Figure 11 is the corresponding curve of the two crucial responses, which can express the quantity and efficiency of the energy absorption.

According to the result in Table 7, it can be seen that the two hydraulic calculation methods results both have good agreement with the drop test results. The maximum discrepancy error is 3.98% in the ground longitudinal force of engineering estimation method result. As shown in Fig. 11, the two numerical simulation corresponding curves considerably have good consistency with the drop test
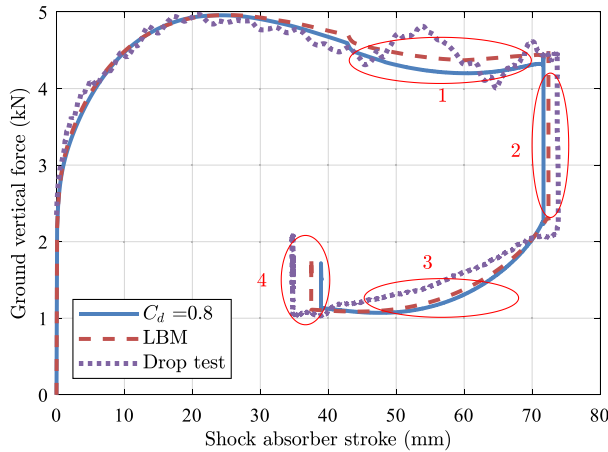
Figure 11. *The ground vertical force curve with shock absorber stroke.*

corresponding curve. Besides, the LBM result is closer to the drop test result in some regions, which are labelled by oval circles in Fig. 11. The hydraulic force gained from the LBM is much higher at a low stroke velocity than the engineering estimation method, which causes the higher ground vertical force in regions 1 and 3. The higher hydraulic force of the engineering estimation method at high stroke velocity leads to the smaller compression stroke as shown in region 2, which brings about a smaller rebound stroke in region 4.

Judging from the comparison results, the engineering estimation method is accurate enough for the industrial application. However, the value of the suitable constant discharge coefficient for a specific landing gear needs the drop test to confirm, which will increase time and economic costs. Besides, the more accuracy of the numerical model will reduce the deviation in the landing gear design process, the LBM can be used to predict the hydraulic force of the shock absorber in landing process.

4.0 Parametric analysis and design

4.1 RS-model and analysis

In this subsection, the response surface method is employed in parallel with the LBM to predict the hydraulic force and the landing response. To acquire the design variables-aircraft landing responses relation for designing a good orifice configuration quickly, the response surface functions are constructed. The construction of the response surface function consists of three steps, including the design of experiment (DOE), response surface fitted, and the analysis of variance (ANOVA).

In this work, five design variables of the landing gear are selected in the design space V shown in Table 8. The research parameters of the landing gear consist of the dimension parameters of the orifice and the properties of the gas chamber. The dimension parameters of the orifice include the diameter of the orifice, the length of the orifice, and the oil compression diameter. Consider the backpressure role on the discharge coefficient, the initial gas volume and gas pressure in the gas chamber of the landing gear are selected as the design variables. The numerical model results are fitted with a quadratic polynomial function using the step-wise regression method in this research [22]. The second-order fitted model [38] relating the response y and the design variables x_i is presented as:

$$y = \beta_0 + \sum_{i=1}^{5} \beta_i x_i + \sum_{i=1}^{5} \beta_{ii} x_i^2 + \sum_{i<j=2}^{5} \sum \beta_{ij} x_i x_j + \varepsilon \tag{15}$$

where denotes a random error spring from the inaccuracy of the model. To obtain a fewer number of sample points while retaining the accuracy of the RS-model, the DOE is constructed based on a

Table 8. *Design variables and design levels in DOE*

Coded value	Variables value increment				
	d_0 (mm)	l_0 (mm)	d_c (mm)	V_0 (mm³)	P_0 (MPa)
−1	3.6	3.0	27.0	123.0	0.80
0	3.8	5.0	28.0	129.5	0.85
1	4.0	7.0	29.0	136.0	0.90

Table 9. *The information of the three landing responses*

Response	Info.	Structural limit for the landing model
η_s	Shock absorber energy absorption efficiency	The larger value is the best
OL	Max overloading of the sprung mass	Smaller than 5G
S	Shock absorber stroke	The lower value is the best

Table 10. *The ANOVA results of RS model for the three responses*

Index	Criteria	Shock absorber efficiency	Max overloading of the sprung mass	Shock absorber stroke
Mean-Squared Error	—	< 0.0001	< 0.0001	0.0004
Sum-Squared Error	—	0.0003	0.0030	0.0094
P-value	< 0.05	< 0.0001	< 0.0001	< 0.0001
R^2	> 0.9	0.9621	0.9853	0.9999
Adj R^2	> 0.9	0.9318	0.9736	0.9999
Adequate precision	> 4	9.4431	16.0750	228.6277

three-level Box-Behnken design, which has 46 sample points. The variables and design levels are shown in Table 8. The shock absorber energy absorption efficiency, max overloading of sprung mass, and the shock absorber stroke are the crucial criteria in characterising the aircraft touchdown performance. The three landing responses are shown in Table 9. The shock absorber efficiency [39] is defined as

$$\eta_s = \frac{\int_0^{S_{\max}} F ds}{S_{\max} F_{\max}} \tag{16}$$

where F denotes the total force in the shock strut. $S_{\max}$ and $F_{\max}$ are the maximum shock absorber stroke and the max total force in the shock strut during landing process.

To examine the accuracy of the fitted model, the four indexes are selected, including P-value, R^2, Adj R^2, and Adequate precision. The calculation methods of indexes are listed in Ref. [22]. The accurate fitted model must satisfy the requirements regarding the four indexes, which are shown in Table 10. Moreover, the scatter points of the numerical model response values versus the predicted values should evenly distribute on both sides of the 45-degree diagonal.

The ANOVA results acquired from the RS-model for the three landing responses are shown in Table 10. The table illustrates that all four indexes for checking the coincidence of the fitted model are meet the criteria. Furthermore, the scatter plots of the numerical model response values versus the predicted values are shown in Fig. 12. These figures demonstrate that the sample points are split evenly by the 45-degree diagonal.

As described in Ref. [22], the response surface models for the three landing responses can be used to simulate the landing response in the design space V. The three RS functions are listed in Table 11. All the functions have three order effects, including the first-order, the second-order, and the interaction effects.

Table 11. *RS functions for the three responses*

| Response	RS function
Shock-strut energy absorption efficiency	$\eta_s = 0.89553 + 0.01034d_0 - 0.01487d_c - 0.00861V_0 + 0.00125P_0 + 0.00386d_0\,d_c - 0.00043d_0\,P_0 - 0.00453d_c V_0 + 0.00064d_c P_0 - 0.00062d_0^2 + 0.00078l_0^2 - 0.0018d_c^2 - 0.00051V_0^2 + 0.00077P_0^2$
Max overloading of the sprung mass	$OL = 3.2805 - 0.05885d_0 + 0.08595d_c - 0.01629V_0 + 0.03655P_0 - 0.01684d_0\,d_c + 0.01752d_c V_0 + 0.00353d_0^2 - 0.00256l_0^2 + 0.00882d_c^2 + 0.00382V_0^2 - 0.00259P_0^2$
Shock absorber stroke	$S = 71.6925 + 0.84751d_0 - 1.2689d_c + 1.9859V_0 - 1.6692P_0 + 0.04315d_0\,d_c + 0.06841d\,V_0 - 0.00707d_0\,P_0 - 0.10053d_c V_0 + 0.00977d_c P_0 - 0.10201V_0 P_0 - 0.02068d_0^2 - 0.02431d_c^2 - 0.04828V_0^2 + 0.02772P_0^2$
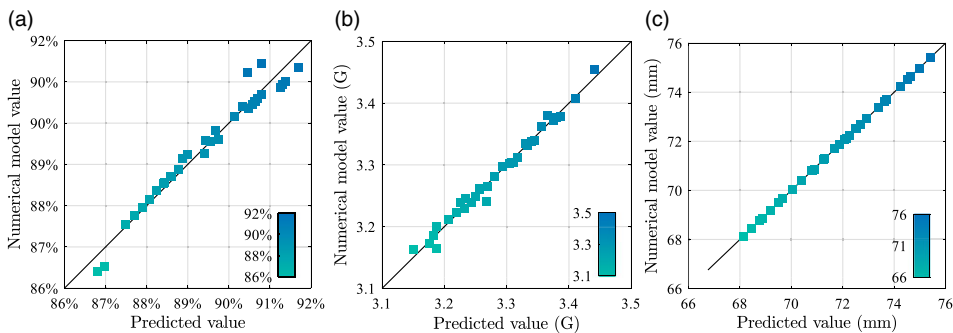
Figure 12. *The numerical model values versus the predicted values of the three responses (a) shock absorber efficiency (b) max overloading of the sprung mass (c) shock absorber stroke.*

4.2 Sensitivity analysis

In this subsection, a global sensitivity analysis based on the Sobol's method is executed to obtain the influence of the design variables on the three landing responses in the design space *V*. According to the theory of Sobol's method [40], the first-order indices represent the sensitivity of the single variable, and the total-effect indices denote all order sensitivity of a variable, including the interaction effects with other variables. The sensitivity analysis results of each design variable under the three RS functions are shown in Fig. 13. Figure 13 shows that the diameter of orifice and the oil compression diameter are the top two sensitive variables for the response η_s and *OL*. It also shows that the initial gas volume and pressure in the gas chamber are the most noticeable sensitive variables for the response *S*. Moreover, all the first-order indices for the three responses take the main part of the corresponding total effect indices.

Figure 14 illustrates the effect of the top two noticeable variables on the three landing responses when the coded values of other variables are set to be zero. Figure 14(a) reveals that the shock absorber efficiency, with an interval of change from 86.40% to 91.44%, increases with the increment of the orifice diameter and the decrement of the oil compression diameter. In accordance with Equation (16), the higher max force in the shock strut leads to a lower shock absorber efficiency. Furthermore, the lower value of the orifice diameter and the higher value of the oil compression diameter contribute to the higher value of the max shock strut force, which will bring about the lower shock absorber efficiency.

Figure 14(b) shows that the max overloading of the sprung mass increases as the oil compression diameter increases and the orifice diameter decreases, with a change interval of 3.16-3.45G. The max overloading is the ratio of the max shock strut force and the value of the sprung mass. The contributions of the orifice diameter and the oil compression diameter on the max shock strut force are reflected in Fig. 14(b).
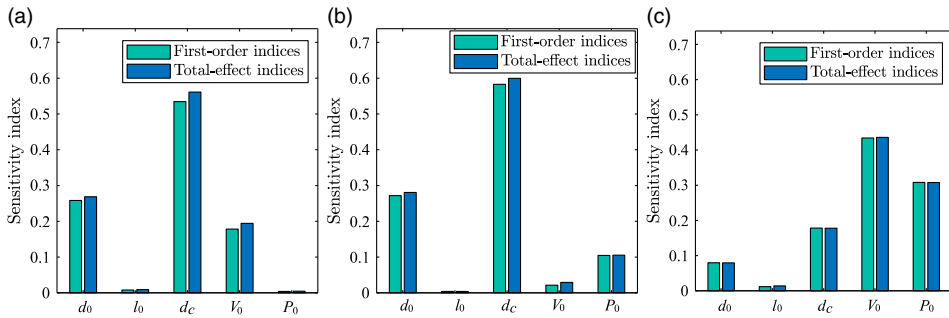
Figure 13. *The sensitivity indices for the three landing responses (a) shock absorber efficiency (b) max overloading of the sprung mass (c) shock absorber stroke.*
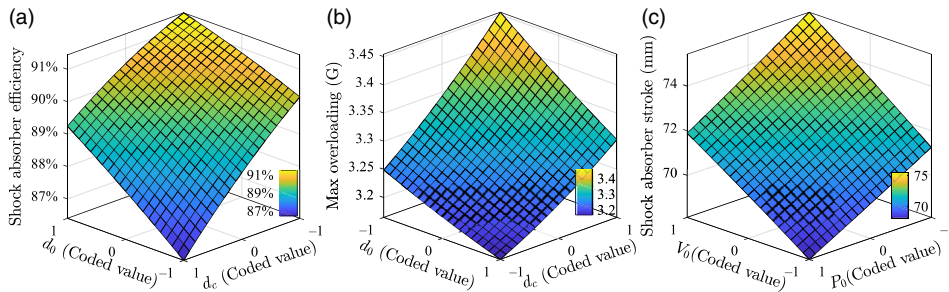

Figure 14. *The top two sensitive variables influence on the three landing responses (a) shock absorber efficiency (b) max overloading of the sprung mass (c) shock absorber stroke.*

Figure 14(c) denotes the effect of the top two noticeable parameters on shock absorber stroke, namely, the initial gas volume and pressure in the gas chamber of the landing gear. Since the functions of the air spring is to limit the compression of the stroke and provide energy to rebound the shock absorber, the high initial gas pressure increases the baseline of the resistance pressure and the low initial gas volume enlarges the increasing speed of the resistance pressure. The change of the shock absorber stroke in the design space is from 68.12 to 75.43mm.

4.3 Optimisation design

Optimisation in this work suggests a philosophical and tactical approach during the design process based on a mathematical representation of the problem (41). A multi-objective optimisation (MDO) is conducted to determine the appropriate value of the design variables of the orifice for a preferable aircraft touchdown performance in this subsection. The MDO is based on the RS functions obtained in Subsection 4.1, which are validated by the numerical model of the landing gear. Figure 15 shows the flowchart of the MDO process. According to the RS functions, the max overloading of the sprung mass and the shock absorber stroke are selected as the optimisation goals in the MDO.

The elitist non-dominated sorting genetic algorithm version II (NSGA-II) is adopted for the optimi-sation [42]. The constraint boundary of design variables is defined in the design space V as shown in Table 8. The mathematical model of the optimisation can be expressed as

$$\min \quad OL, S$$
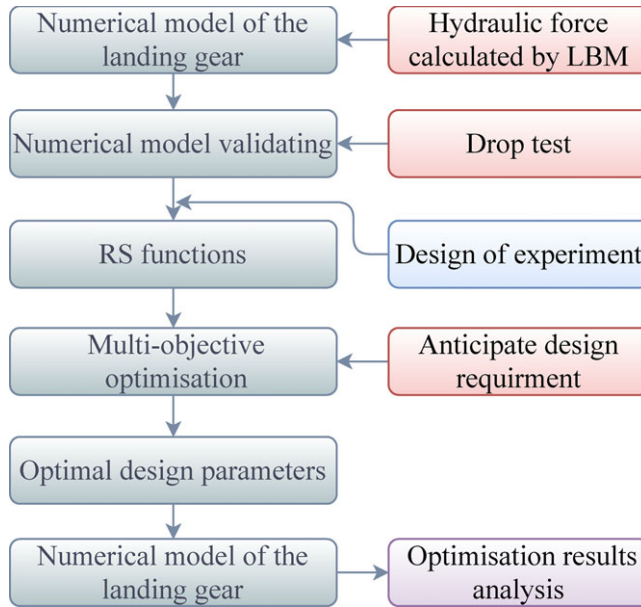$$s.t. \quad [d_0 , l_0 , d_c , V_0 , P_0] \in V \tag{17}$$

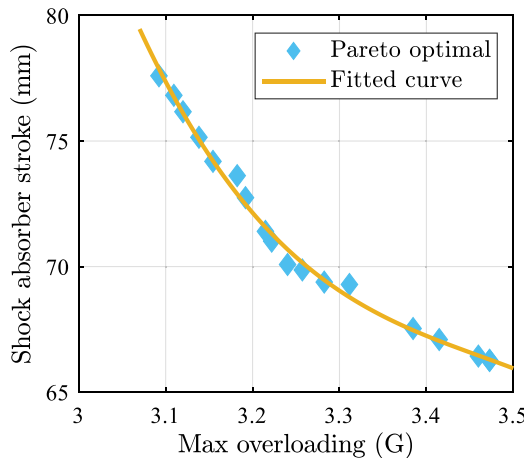**Figure 15.** *Flowchart of the MDO process.*

Figure 16. *The Pareto front of two optimisation goals.*

After the optimisation, the Pareto front of the optimisation results fitted by the two optimisation goals is shown in Fig. 16. To keep the comparability of the optimisation results, the optimum values of the design parameters are selected from the Pareto front around the area where the shock absorber stroke equal to the value before the optimisation. The optimum coded values and actual values of the design variables of the orifice and the gas chamber are shown in Table 12. The orifice structure is modified based on the optimisation results and is used in calculating the hydraulic force with the LBM. The simulation results of the numerical model of the landing gear under the same landing condition are shown in Table 13.

Table 13 compares the landing response results before and after optimisation. It can be seen that the shock absorber stroke retains almost the same value as the original value after optimisation. Besides, the max overloading of sprung mass decreases by 5.44% as the shock absorber efficiency increases

Table 12.   *The optimised values of the landing gear variables*

Info.	d_0	l_0	d_c	V_0	P_0
Coded value	0.6156	0.9306	–0.9411	–0.7692	0.1812
Actual value	3.9231mm	6.8612mm	27.0589mm	124.5003mm^3	0.8591MPa

Table 13.   *Comparison of the optimisation results*

Info.	Before	After	Variation
Shock-strut efficiency	89.55%	91.03%	1.65%
Max overloading (G)	3.31	3.13	−5.44%

by 1.65%. The touchdown performance still gets some improvement after optimisation even the shock absorber efficiency is already at a high level in the original layout of the landing gear.

5.0 Conclusions

Based on the feature of the damping orifice, the lattice Boltzmann method is used to simulated the flow characteristic of the sharp-edged orifice. The simulation results of a computation example of the sharp-edged orifice are compared with the published experimental results. The sharp-edged damping orifice analysis is carried out with the hydraulic force calculated by the LBM. The simulations under different turbulence models show that LBM with WALE turbulence model has a higher feasibility for simulating damping orifice flow, with the lowest maximum relative error value of 7.07%. The analysis results of the damping orifice denote that the hydraulic force increases with the decrement of the orifice diameter and the increment of the oil compression diameter.

The numerical model of the landing gear for predicting the aircraft landing response is established. The drop test of single landing gear is carried out to validate the accuracy of the numerical model. The results show that the engineering estimation method and the LBM can both be used to calculate the hydraulic force of the landing gear. But the more accuracy of the LBM is preferable for the parametric analysis of the damping orifice in the design process.

The RS functions of the landing responses are constructed based on the numerical model of the landing gear for the parametric analysis on the damping orifice. The sensitivity analysis and the optimisation design are carried out based on the RS functions. The ANOVA results show that the RS functions simulated the landing response effectively and can be used to predict the landing response. The most noticeable variables for the three landing responses in the design space *V* are the oil compression diameter, the oil compression diameter, and the initial gas volume respectively. The max overloading of the sprung mass decreases by 5.44% after the optimisation even the shock absorber efficiency is already at a high level in the original layout of the landing gear. The analysis and optimisation results show that the LBM coupled with RSM is a feasible methodology to design the parameters of damping orifice for good landing performance. This analysis and design optimisation method can be used for the general design of oleo-pneumatic shock absorber with fixed cross-sectional area damping orifice.

References

[1] Krüger, W., Besselink, I., Cowling, D., Doan, D.B., Kortüm, W. and Krabacher, W. Aircraft landing gear dynamics: simulation and control, *Vehicle Syst. Dyn.*, 1997, **28**, (3), pp 119–158.
[2] Milwitzky, B. and Cook, F.E. Analysis of landing-gear behavior NACA-TN-2755, National Advisory Committee for Aeronautics, Hampton, VA, USA, 1953.
[3] Sartor, P., Worden, K., Schmidt, R.K. and Bond, D.A. Bayesian sensitivity analysis of flight parameters that affect main landing gear yield locations, *Aeronaut. J.*, 2014, **118**, (1210), pp 1481–1497.

[4] Jo, B., Jang, D., Hwang, J. and Choi, Y. Experimental validation for the performance of MR damper aircraft landing gear, *Aerospace*, 2021, **8**, (9), pp 272.

[5] Gao, Z. *Aircraft Design Manual: Take-Off and Landing System Design*. Aviation Industry Press, Beijing, 2002.

[6] Essien, S., Archibong-Eso, A. and Lao, L. Discharge coefficient of high viscosity liquids through nozzles, *Exp. Therm. Fluid Sci.*, 2019, **103**, pp 1–8.

[7] Jamei, M., Ahmadianfar, I., Chu, X. and Yaseen, Z.M. Estimation of triangular side orifice discharge coefficient under a free flow condition using data-driven models, *Flow Meas. Instrum.*, 2021, **77**, pp 101878.

[8] Jiang, L., Liu, Z. and Lyu, Y. Internal flow and discharge coefficient characteristics of oil jet nozzles with different orifice angles under non-cavitating conditions, *Aerosp. Sci. Technol.*, 2021, **110**, pp 106473.

[9] Ding, Y.W., Wei, X.H., Nie, H. and Li, Y.P. Discharge coefficient calculation method of landing gear shock absorber and its influence on drop dynamics, *J. Vibroeng.*, 2018, **20**, (7), pp 2550–2562.

[10] Tharakan, T.J. and Rafeeque, T.A. The role of backpressure on discharge coefficient of sharp edged injection orifices, *Aerosp. Sci. Technol.*, 2016, **49**, pp 269–275.

[11] Yu, B., Fu, P.F., Zhang, T. and Zhou, H. The influence of back pressure on the flow discharge coefficients of plain orifice nozzle, *Int. J. Heat Fluid Fl.*, 2013, **44**, pp 509–514.

[12] Yu, H., Zhu, P., Suo, J. and Zheng, L. Investigation of discharge coefficients for single element lean direct injection modules, *Energies*, 2018, **11**, (6), pp 1603.

[13] Payri, F., Bermúdez, V., Payri, R. and Salvador, F.J. The influence of cavitation on the internal flow and the spray characteristics in diesel injection nozzles, *Fuel*, 2004, **83**, (4–5), pp 419–431.

[14] Ling, J. and Templeton, J. Evaluation of machine learning algorithms for prediction of regions of high Reynolds averaged Navier Stokes uncertainty, *Phys. Fluids*, 2015, **27**, (8), pp 85103.

[15] Chen, S. and Doolen, G.D. Lattice Boltzmann method for fluid flows, *Annu. Rev. Fluid Mech.*, 1998, **30**, (1), pp 329–364.

[16] Thibault, S., Holman, D., Garcia, S. and Trapani, G. CFD Simulation of a quad-rotor UAV with rotors in motion explicitly modeled using an LBM approach with adaptive refinement. *55th AIAA aerospace sciences meeting*, Grapevine, Texas, USA, 2017, pp 583.

[17] Zhang, R., Kim, H. and Dinoy, P.R. Particle flow simulation based on hybrid IMB-DEM-LBM approach with new solid fraction calculation scheme, *Appl. Sci.*, 2021, **11**, (8), pp 3436.

[18] Xu, A., Zhao, T.S., An, L. and Shi, L. A three-dimensional pseudo-potential-based lattice Boltzmann model for multiphase flows with large density ratio and variable surface tension, *Int. J. Heat Fluid Fl.*, 2015, **56**, pp 261–271.

[19] Wang, Y., Shu, C. and Yang, L.M. An improved multiphase lattice Boltzmann flux solver for three-dimensional flows with large density ratio and high Reynolds number, *J. Comput. Phys.*, 2015, **302**, pp 41–58.

[20] Holman, D.M., Brionnaud, R.M., Modena, M.C. and Sánchez, E.V. Lattice Boltzmann method contribution to the second high-lift prediction workshop, *J. Aircraft*, 2015, **52**, (4), pp 1122–1135.

[21] Lin, T., Xia, W. and Hu, S. Effect of chordwise deformation on propulsive performance of flapping wings in forward flight, *Aeronaut. J.*, 2021, **125**, (1284), pp 430–451.

[22] Myers, R.H., Montgomery, D.C. and Anderson-Cook, C.M. Response Surface Methodology: Process and Product Optimization using Designed Experiments. John Wiley & Sons, Hoboken, NJ, USA, 2016.

[23] Yang, X., Xing, Y., Zhang, Z., Yang, J. and Sun, Y. Theoretical analysis and multi-objective optimisation for gradient engineering material arresting system, *Int. J. Crashworthines.*, 2017, **22**, (5), pp 541–555.

[24] Wang, C., Nie, H., Chen, J. and Lee, H.P. Damping force analysis and optimization of a lunar lander with MRF, *J. Aerospace Eng.*, 2020, **33**, (3), pp 4020004.

[25] Ding, Z., Wu, H., Wang, C. and Ding, J. Hierarchical optimization of landing performance for lander with adaptive landing gear, *Chin. J. Mech. Eng.*, 2019, **32**, (1), pp 1–12.

[26] Krause, M.J., Kummerländer, A., Avis, S.J., Kusumaatmaja, H., Dapelo, D., Klemens, F., Gaedtke, M., Hafen, N., Mink, A., Trunk, R., Marquardt, J.E., Maier, M., Haussmann, M. and Simonis, S. OpenLB—Open source lattice Boltzmann code, *Comput. Math. Appl.*, 2021, **81**, pp 258–288.

[27] D'Humières, D. Multiple-relaxation-time lattice Boltzmann models in three dimensions, *Philos. Trans. A Math. Phys. Eng. Sci.*, 2002, **360**, (1792), pp 437–451.

[28] McCracken, M.E. and Abraham, J. Multiple-relaxation-time lattice-Boltzmann model for multiphase flow, *Phys. Rev. E*, 2005, **71**, (3), pp 36701.

[29] Weickert, M., Teike, G., Schmidt, O. and Sommerfeld, M. Investigation of the LES WALE turbulence model within the lattice Boltzmann framework, *Comput. Math. Appl.*, 2010, **59**, (7), pp 2200–2214.

[30] Smagorinsky, J. General circulation experiments with the primitive equations: I. The basic experiment, *Mon. Weather Rev.*, 1963, **91**, (3), pp 99–164.

[31] Germano, M., Piomelli, U., Moin, P. and Cabot, W.H. A dynamic subgrid-scale eddy viscosity model, *Phys. Fluids A Fluid Dyn.*, 1991, **3**, (7), pp 1760–1765.

[32] Ducros, F., Nicoud, F. and Poinsot, T. Wall-adapting local eddy-viscosity models for simulations in complex geometries, *Numerical Methods for Fluid Dynamics VI*, 1998, pp 293–299.

[33] Menter, F.R. Two-equation eddy-viscosity turbulence models for engineering applications, *AIAA J.*, 1994, **32**, (8), pp 1598–1605.

[34] Khapane, P.D. Simulation of asymmetric landing and typical ground maneuvers for large transport aircraft, *Aerosp. Sci. Technol.*, 2003, **7**, (8), pp 611–619.

[35] Marques, F., Flores, P., Claro, J.C.P. and Lankarani, H.M. Modeling and analysis of friction including rolling effects in multibody dynamics: a review, *Multibody Syst. Dyn.*, 2019, **45**, (2), pp 223–244.

[36] Wen, Z., Zhi, Z., Qidan, Z. and Shiyue, X. Dynamics Model of carrier-based aircraft landing gears landed on dynamic deck, *Chinese J. Aeronaut.*, 2009, **22**, (4), pp 371–379.

[37] Li, Y., Jiang, J.Z., Neild, S.A. and Wang, H. Optimal inerter-based shock–strut configurations for landing-gear touchdown performance, *J. Aircraft*, 2017, **54**, (5), pp 1901–1909.

[38] Vadde, K.K., Syrotiuk, V.R. and Montgomery, D.C. Optimizing protocol interaction using response surface methodology, *Ieee T. Mobile Comput.*, 2006, **5**, (6), pp 627–639.

[39] Han, C., Kang, B., Choi, S., Tak, J.M. and Hwang, J. Control of landing efficiency of an aircraft landing gear system with magnetorheological dampers, *J. Aircraft*, 2019, **56**, (5), pp 1980–1986.

[40] Sobol, I.M. Global sensitivity indices for nonlinear mathematical models and their Monte Carlo estimates, *Math. Comput. Simulat.*, 2001, **55**, (1), pp 271–280.

[41] Papalambros, P.Y. and Wilde, D.J. *Principles of optimal design: modeling and computation*. Cambridge University Press, Cambridge, UK, 2000.

[42] Deb, K. *Multi-Objective Optimization using Evolutionary Algorithms: An Introduction*. Springer, London, UK, 2011.